Screening of EOR potential on the pore scale by statistical and topological means

Holger Ott[1*], *Ahmad* Kharrat[1], *Mostafa* Borji[1], *Thorsten* Clemens[2], *Pit* Arnold[1]

[1]Department Petroleum Engineering, Montanuniversität Leoben, 8700 Leoben, Austria.
[2]OMV E&P, Vienna, Austria.

Abstract. Chemical EOR processes modify properties of fluid-fluid and rock-fluid interfaces in the pore space with the aim of mobilizing additional oil. The initial mobilization takes place on the scale of the individual pore. Therefore, observations on the pore scale provide valuable insights into water-oil displacement mechanisms; the understanding of these mechanisms enables an efficient design of the injection water chemistry. In this article, we present a first step towards a statistical and topological fingerprint of EOR processes used to characterize and optimize EOR processes. We use microfluidics to observe changes in the oil distribution in the pore space and the formation of emulsion phases. The oleic phase was analyzed by statistical and topological means showing a systematic change as a function of alkali concentration. In particular, Lorenz diagrams and the normalized Euler characteristic appeared as sensitive to changes in the water chemistry. It turned out that the displacement processes are influenced by emulsion formation, especially at low and high alkali concentrations. This is implicitly reflected in the statistical and topological analysis, but has not yet been explicitly taken into account.

1 Introduction

Alkaline flooding is a chemical Enhanced Oil Recovery (EOR) method, which is often combined with surfactant and polymer flooding [1-3]. The addition of an alkaline agent to the injection water results in a high pH and can lower the interfacial tension when the crude contains a substantial amount of fatty acids, which is reflected in the total acid number (TAN). At high pH values, hydroxide ions and acidic oil components saponify at the oil-water interface, resulting in the generation of in-situ surfactants. The resulting decrease in interfacial tension commonly leads to emulsification and an increasing displacement efficiency, leading to additional oil recovery.

Complex chemical EOR processes such as alkali or surfactant flooding are typically optimized for their phase behavior and by conventional core flooding experiments. However, the information from core floods is rather limited, as there are no direct insights into details of oil mobilization and displacements. As a rule, cumulative oil production and differential pressure are measured. These are rather one-dimensional information from which complex displacement processes must be understood. On the other hand, the phase behavior, respectively the degree of emulsification, is often analyzed in test-tubes and not under realistic flow, respectively mixing conditions as in porous media.

Chemical EOR processes modify fluid-fluid and rock-fluid interfacial properties in the pore space in order to mobilize additional oil. There are several techniques by which oil mobilization can directly be observed in the pore space, such as micro-CT imaging [4, 5] and microfluidics [6-9]. It has further been demonstrated that both techniques, but especially microfluidics, allow as well the identification of emulsion phases and hence give access to combined information on flow and phase behavior [7, 9].

In the recent years, fluid distributions on the pore scale have been analysed by statistical and topological means, deriving information that is more sophisticated and may provide more insight into EOR displacements than e.g. recovery curves and differential pressure measurements alone. Cluster-volume and cluster-length distributions have been used to characterize fluid phases and have been linked to fluid-phase mobility [4, 5, 10-12]. These distributions are characteristic, but their interpretation with respect to oil mobility depends on the tail end of the distribution, which may be influenced by the limited field of view [11], respectively the largest clusters that may not be statistically represented in the observed volume. However, the distributions themselves are fairly independent of the tail end and thus of the field of view and may be robust displacement characteristics.
Another very recent development is the description of the microscopic fluid-phase distribution by topological means using Minkowski functionals [13, 14]. Fluid phase topology is linked to classical parameters like fluid saturation, capillary pressure, capillary pressure hysteresis and the wetting state [14, 15]. The advantage of a topological description is that it assigns these parameters a well-defined physical and mathematical meaning. Of particular interest in this context is the Euler characteristic, which describes the connectivity of a fluid phase and may be associated with wetting properties [14].

In the frame of the present study, we investigate displacements of crude oil by water and alkali solutions. We use microfluidics (MF) to screen the performance of the injection water as a function of alkali concentration.

* Corresponding author: holger.ott@unileoben.ac.at

The advantage of using MF for EOR screening is (a) that MF devices are chemically very well defined, (b) that MF experiments are relatively fast performed and cost competitive, and (c) MF can easily be parallelized and is therefore an ideal screening tool. There are of course shortcomings with respect to interactions of fluids with mineral phases and with mimicking realistic rock structures. In the present work, we focus on fluid-fluid interactions and use therefore MF according to its strength.
We take advantage of the high spatial and temporal resolution achievable in MF to observe fluid displacement processes like the breaking of oil clusters, changes of wetting states and the formation of emulsion phases. We analyze fluid-phase distributions by means of a statistical and topological description of oil clusters, and link the observations to the injection water chemical composition.

The study shows (a) that cluster analysis can be used for EOR screening, which is a first step towards a statistical fingerprinting for optimizing EOR processes, (b) that classical phase-behavior experiments do not reflect the phase behavior under flow conditions, and (c) that emulsion formation might be of disadvantage and may lead to oil phase pinning.

2 Materials and methods

2.1. Porous medium

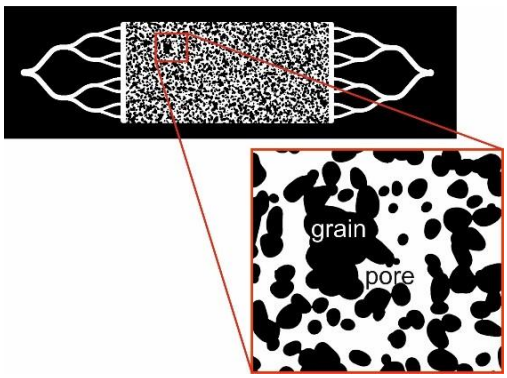

Fig. 1: 2D pore structure etched in glass microfluidic chips. The porous domain is contacted on the left and right by channel systems for fluid injection and production resulting in a linear flow geometry.

Experiments were performed with microfluidic chips made from borosilicate glass, representing a 2D porous media. The pattern is characterized by a homogeneous etching depth of 20 µm and a lateral definition of pores and pore throats. Porosity and permeability have been determined to $\phi = 0.57$ and $K = 2.5$ D and total pore volume to 2.3 μl. The total porous domain is 1 cm × 2 cm with channel systems at the inlet and outlet for a proper fluid distribution and fluid collection as displayed in Fig. 1. The lateral porous structure is rather open and homogeneous with all features larger than the etching depth, and with the simulated capillary pressure curve showing an extended plateau.

2.2 Instrumentation

The flooding experiments were performed at ambient conditions with a constant flow rate boundary condition at the inlet, and a constant pressure boundary condition at the outlet. Fluids were injected with a high precision Chemyx Fusion 200 syringe pump. For each fluid type, a separate syringe was used. On the downstream side, a constant pressure boundary condition was realized by producing fluids into a vessel at atmospheric pressure. For preparation purpose, a vacuum pump was installed on the downstream side to evacuate the micromodel and the flow lines, and for pre-saturation.
For imaging the fluid phases in the pore space, a Leica DMi 8 high-end microscope with a wide-range automated xy table and an image stitching option was used, providing a high spatial resolution and a time resolution that allows for detailed investigation of displacement processes and fluid phase configurations. The images were recorded with a Leica DMC2900 camera.

2.3 Fluids

Experiments with three different oil samples from the Vienna Basin were performed in order to investigate the variability of displacement patterns in water flooding. The samples were characterized by the viscosity (µ), interfacial tension to water (IFT) and the total acid number (TAN) as listed in Table 1. The bulk of experiments and all alkaline floods have been performed with crude 8. As injection water, deionized (DI) water was used. Alkaline solutions were prepared on basis of DI water with Na_2CO_3 as alkali agent in concentrations in between 200 ppm and 12000 ppm. In this range, the pH varies monotonically in between 10.6 and 11.6 as shown in Table 1. IFT of Crude 8 to the various alkaline solutions are not reported here; emulsion phases separate in the capillary of the spinning-drop tensiometer, leading to an instable three-phase system making a reliable IFT measurement impossible. However, the phase behavior indicates that IFT monotonically decreases with increasing alkali concentration leading to an increasing miscibility.

Table 1: Crude oil properties; IFT was measured to DI water by spinning-drop tensiometry. The API gravity indicates medium heavy oil. Crude 8 and 16 show relatively high TAN, which indicates that the respective fields are potential targets for alkaline flooding. Bottom row: measured pH of water as function of the Na_2CO_3 concentrations.

Crude	Viscosity [cP] at 20 °C	IFT [mN/m] at 20 °C	TAN [mg KOH /g oil]	API Gravity [°]
8	331	0.7±0.1	1.96	19.88
16	80	12.7±1	1.56	23.79
F	not measured	5.5±0.7	0.34	30.14
Inj. water pH	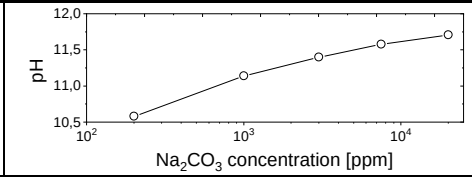			

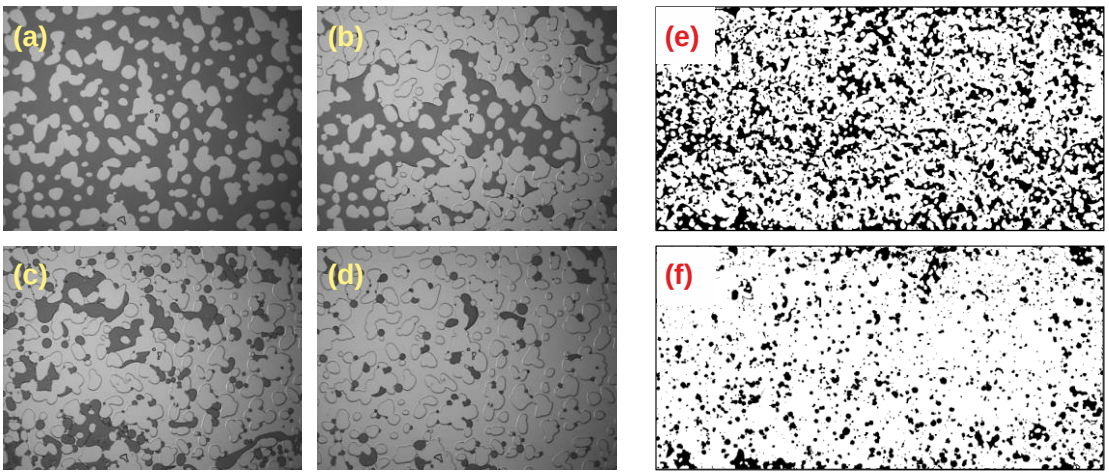

Fig. 2: Left images: Water flood and subsequent alkaline flood with a Na_2CO_3 concentration of 950 ppm. (a) to (d): images of a subvolume during an experimental sequence. (a) oil saturated micromodel, (b) the same section during water flooding, (c) during alkaline flooding and (d) after alkaline flooding. Right images: Segmented images showing the oil phase in black. The images cover the total flooding domain. Image (e) was taken after water flooding and (f) after alkaline flooding.

2.4 Sample preparation

The microfluidic chips were cleaned before each experiment by injecting 250 pore volumes (PV) of distilled water at high flow rate and subsequently a sequence of solvents at low flow rate to allow for efficient displacement and mixing with the fluids in place: 50 PV of acetone followed by 50 PV of toluene followed by another 50 PV of acetone to clean out the toluene. In a final step, vacuum was applied to vaporize the acetone. After cleaning, no fluids or colouring were visible in the micromodels, nor in the injection and production lines. After cleaning, oil was injected under vacuum conditions until the sample was oil saturated – no connate water was present at the beginning of the experiments.

2.5 Flooding experiments

The starting point of each experiment was a fully oil saturated sample with $S_o = 1$. To mimic a tertiary recovery process, firstly water was injected immiscibly displacing oil from the porous domain. The flooding time was always in between 22 h to 24 h, longer than the time to reach steady stead with no detectable change of the oil saturation in the porous medium at the end of each flood. Subsequently, the samples were flooded with alkaline solutions in order to study tertiary displacement effects. The alkaline-flooding time did not exceed 24 h either. For both, water and alkaline flooding, an injection rate of 0.01 ml/h have been chosen, leading to an interstitial velocity of about $2.4 \cdot 10^{-5}$ m/s (~ 6.9 ft/day). The total injected volume corresponds to approximately 100 PV. This relatively high flow rate corresponds to velocities in the vicinity of injection wells, where initial oil mobilization may take place prior to oil-bank formation.

Optical images of the flood domain were taken under flow conditions; in some cases, with a relatively small field of view and a high time resolution of about 100 ms to 1 s, in most cases with a field of view that covered the entire flood area with high spatial resolution, resulting in a lower time resolution of the order of 30 s to 1 min. The statistical and topological analysis was carried out mainly on the final image in the stationary state.

3 Fluid displacements – visual observations

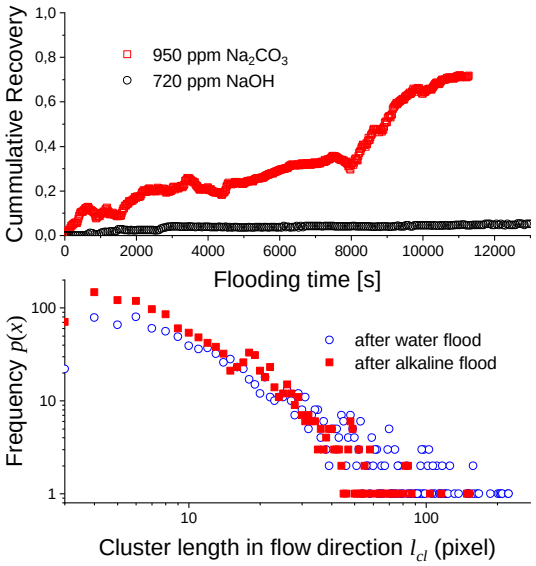

Fig. 3: Top panel: tertiary recovery curves of alkaline flooding with 950 ppm Na_2CO_3 and 720 ppm NaOH. The data were calculated from the subvolume in the left panel in Fig. 2. Bottom: cluster length distributions of experimental sequences: water followed by alkaline flooding.

The left panel of Fig. 2 shows typical microscopic images of a subvolume during an experimental sequence. The initial state of all experiments is $S_o = 1$ as shown in (a). The "grains" appear in light grey and the oil saturated pore volume in dark grey with a good optical contrast for image segmentation. To study tertiary recovery processes, the samples are at first water flooded to a state close to residual saturation as shown in Fig. 2 (b). During water flooding, water is invading by displacing the oil. Remaining larger clusters are pinned to the "grains" as a result of the initial "oil-wet" state. In time, larger clusters break down by snap-off effects producing smaller

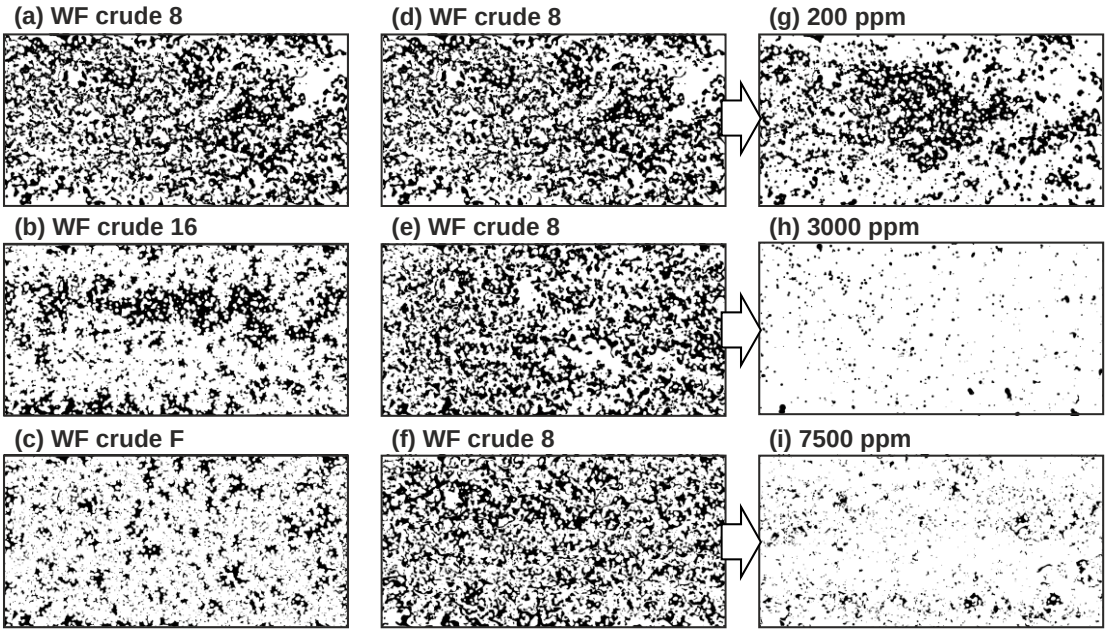

Fig. 4: Left: Secondary water floods of three different crude oils. Middle: Secondary water floods of crude 8; three repeat experiments at identical conditions. Right: Tertiary floods in sequence to the water floods in the respective left image (middle column). The alkali agent was Na_2CO_3 with concentrations of 200, 3000 and 7500 ppm.

droplets/ganglia that are mobile and are produced by the injected water. After a certain time, a steady state is reached, with a stationary remaining oil phase.

During the subsequent injection of an alkalic solution with 950 ppm Na_2CO_3 [16], interfacial tension between oil and water is lowered and the remaining clusters break further down with the fragments being produced. As a result, after alkaline flooding, the oil saturation is substantially lower, and the oil-cluster sizes are further reduced. The respective tertiary production curve is shown in the upper panel of Fig. 3; the data is calculated from the time dependent saturation states of the subvolume shown in Fig. 2 (b) to (d).

The lower panel of Fig. 3 shows the cluster length distribution $p(l_{cl})$ determined from the whole flooding domain (Fig. 2 (e) and (f)) after water and alkaline flooding, respectively; the breakdown of the clusters is reflected in the change of $p(l_{cl})$ to a larger number of smaller, and a smaller number of larger clusters, resulting in a narrower distribution after EOR.

3.1 Final displacement patterns and repeatability

Repeating individual experiment did not result in exactly the same displacement pattern and recovery factor. What means "being repeatable"? The middle column of Fig. 4 compares the oil saturations after water flooding performed with the same fluids under the same conditions. The patterns show some similarity, but are different. To spot the similarity, we compare them to displacement patterns obtained for different crude oils under otherwise the same conditions (crude properties are listed in Table 1). Comparing the displacement patterns, some statements can be made, e.g. that crude 16 with highest interfacial tension to water shows the most heterogeneous displacement pattern, with large clusters dominating the oil saturation. In general, we observe substantially different displacement patterns for the different crude oils. Repeat experiments with crude 8 (middle column) show in comparison relatively homogeneous and similar patterns. All the following experiments were performed with crude 8.

The final displacement pattern after tertiary flooding with 200, 3000, 7500 ppm Na_2CO_3 solutions are shown in the right column of the same figure. The final oil saturations, i.e. the displacement efficiencies, varies substantially as indicated by the respective black covered areas. While at 200 ppm some additional oil is recovered, the displacement efficiency appears to be best at 3000 ppm. For the two higher concentrations, the trend to smaller cluster sizes is observed.

3.2 Effects of emulsification

An important and noteworthy observation is that under flow conditions only very little emulsion formation was observed. This is in contrast to phase-behavior experiments which show strong emulsification. Under flow conditions, emulsion phases formed at relatively low and high concentrations, i.e. outside the optimum. This can be explained by the intensity of the contact between the oil and the alkali agent taking into account the alkali concentration and the contact time between the phases.

The effect of emulsification may be illustrated for low, but comparable concentration of NaOH (720 ppm in DI water), which is a stronger alkali agent, in comparison to the case discussed above (950 ppm Na_2CO_3) [16]. Under otherwise the same conditions, minor oil production was observed, associated with stagnant oil clusters and slow but extensive formation of an emulsion phase. Microemulsions are known to allow extremely low interfacial tension between oil and water, but have a high

viscosity, which may be detrimental to displacement efficiency. In the present case, microemulsions form at the oil-water interfaces and appear to be immobile and pin clusters in the pore space. Even if the clusters break by snap off, the fragments remain largely immobile, resulting in a low tertiary recovery factor (Fig. 3).

4 Recovery factors

4.1 Displacement process

After water flooding, the remaining oil phase is dominated by rather large oil clusters as can be seen in Fig. 2 (b) and (e). The system appears as partially wetted by water and partially by oil and may be described as mixed wet. In this specific experiment, an oil recovery of 0.52 has been reached. During subsequent alkaline flooding, these clusters broke down in droplets, which appeared to be mobile and are displaced by the injection water and 0.72 of the afore remaining oil was recovered. In comparison to the water flood, the remaining oil phase after alkaline flooding can rather be described by small dispersed droplets that are trapped in the pore structure.

4.2 Recovery calculations

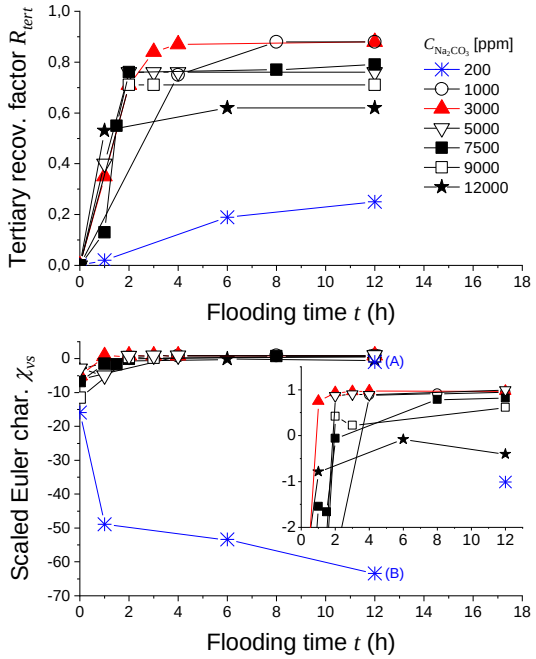

Fig. 5: Top: recovery factors, $\boldsymbol{R_{tert}}$, as function of flooding time for different Na_2CO_3 concentrations. Bottom: the respective normalized Euler characteristic. (A) and (B) correspond to different interpretations of the 200-ppm experiment as described in the text. The inset shows a zoon-in of the main panel.

The recovery factors of the secondary water floods, R_{sec}, were calculated from the remaining oil in the pore space, represented by the dark area, A_{oil}, after image segmentation: $R_{sec} = 1 - \frac{A_{oil}}{A_{pore}}$, where A_{pore} corresponds to the porosity, which is measured from the initial state, $S_o = 1$, in the same way as later A_{oil}. For tertiary floods, we calculate the additionally recovered oil R_{tert}, which is defined as: $R_{tert} = 1 - \frac{A_{oil}}{A_{oil,sec}}$, and which refers to the volume of oil in place after the preceding water flood.

The recovery curves show differences in the displacement efficiency for different Na_2CO_3 concentrations; in the upper panel of Fig. 5, R_{tert} is plotted as function of time. Different ultimate recoveries as well as different time dependencies were observed; while, e.g., at 1000 ppm and 3000 ppm similar ultimate recovery factors were reached, the 3000-ppm recovery curve appears steeper and ultimate recovery was reached much earlier. Above and below this range, ultimate recovery decreases.

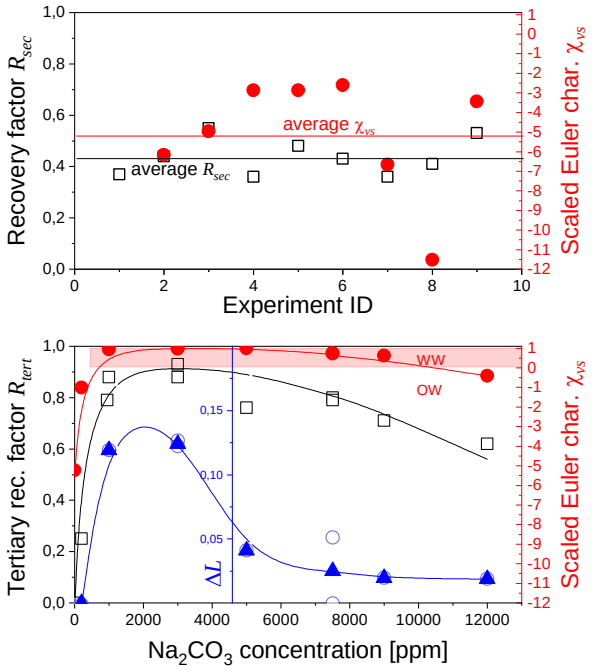

Fig. 6: Top: recovery factors (volumetric property) and the normalized Euler characteristic (topological property) after water-flooding experiments performed under identical conditions. Bottom: the same quantities for alkaline experiments as a function of the Na_2CO_3 concentration. The blue Symbols represent the difference in the Lorenz factor $\boldsymbol{\Delta L}$ as calculated from the cluster-volume distribution (statistical property).

Fig. 6 shows the ultimate recovery factors after water flooding (top panel) and after alkaline flooding (bottom panel). The recovery factor by water flooding varies with an average of 0.43 (±0.1) with a standard deviation of 0.1. The scatter may be a result of the relatively small flooding domain; the porosity-based REV of the used micromodel corresponds to an area of $5 \times 5\ mm^2$, which is smaller than the total flooding domain of $20 \times 10\ mm^2$. However, it is known that in two-phase flow, the REV can be larger, not only depending on the pore structure, but also on the distribution of the fluids therein [11]; if a system is dominated by large oil clusters, the cluster-size distribution may be truncated by the system size, or the largest clusters are not statistically represented in the flooding domain. In these cases, the observed recovery factor may still be scale dependent.

The bottom panel of Fig. 6 shows the final tertiary recovery factor as a function of Na_2CO_3 concentration. According to the definition, at zero concentration, no additional oil is recovered. With increasing Na_2CO_3 concentration, the recovery factor increases steeply with a maximum in the range between 1000 to 3000 ppm. At higher concentrations, the recovery factor decreases again. This behaviour will be further characterized in terms of wettability and is affected by emulsion formation. After alkaline flooding, the oil cluster sizes are generally smaller, and the REV is therefore smaller than for the respective water flood.

5 Euler Characteristic

From Fig. 2 it becomes obvious that the wetting state of the sample changes during the experimental sequence. Initially, the system is in an oil wet state. This is due to the fact, that we start the experiments with $S_o = 1$ and oil is initially wetting the glass surface. During water flooding, oil is partially displaced by water. In the swept areas, wettability changes to a more water-wet state, however, large clusters are still connected over several pores, partially covering the "grains" – we may call this a mixed-wet system. During alkaline flooding, larger clusters are pinned by their contacts to the grains, but successively break up by viscous forces into smaller non-wetting droplets; the system turns successively water wet where internal surfaces got in contact with the injection water.

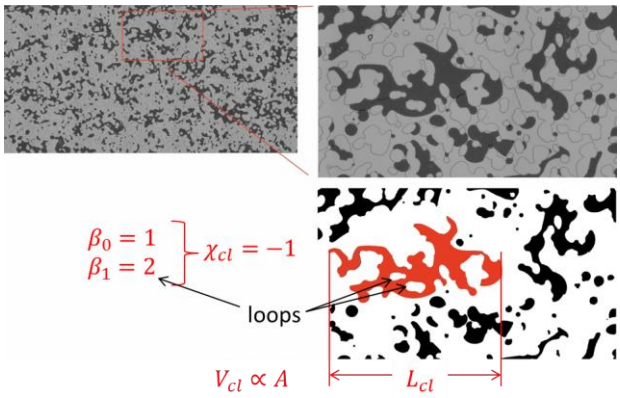

Fig. 7: Determination of cluster properties. Left: oil distribution after a water flood. Right: zoom-in and corresponding segmented image. The red labeled oil cluster has a Euler characteristic of $\boldsymbol{\chi_{cl} = -1}$, corresponding to one object and two loops.

It has recently been shown that the wetting state is closely linked to the Euler characteristic (χ), which describes the connectivity of a fluid phase [14]. In the following, we make use of this link to characterize the change of the wetting state during displacements. The Euler characteristic, χ, can be calculated from the Betti numbers, β_i: $\chi = \beta_0 - \beta_1 + \beta_2$. β_0 refers to the number of objects, i.e., the number of clusters in the system, β_1 is the number of loops or holes in the structure and β_2 refers to the number of inclusions. In 2D systems, inclusions do not exist and $\beta_2 = 0$.

According to the definition, χ scales with the number of objects, and tiny droplets may contribute with the same weight as large clusters, which are more significant for oil production. Therefore χ is not a good measure in the present case, because recovery does not refer to the number of objects, but to oil volumes, and larger clusters contribute more than small droplets. We therefore propose an alternative Euler characteristic, χ_{vs}, scaled by cluster volumes:

$$\chi_{vs} = \frac{\sum_{n_{cl}} \chi_{cl} V_{cl}}{\sum_{n_{cl}} V_{cl}},$$

with n_{cl} being the number of clusters, χ_{cl} the Euler characteristic of an individual cluster and V_{cl} the volume of this cluster. As a result, the most water-wet state corresponds to individual droplets with $\chi_{cl} = 1$ and has $\chi_{vs} = 1$. The most oil wet state then corresponds to $\chi_{vs} = 1 - N_{grains}$ with N_{grains} being the number of "rock grains", which is then equal to the number of loops. The determination of χ_{cl} is illustrated in Fig. 7.

The evaluated χ_{vs} after the different water and alkaline floods have been plotted together with the recovery factors in Fig. 6. Referring to oil wet as $\chi_{vs} < 0$ and to water wet as $\chi_{vs} > 0$, we can state that after water flooding, generally an oil-wet behavior has been observed, changing towards a more water-wet state during alkaline flooding. This development $\chi_{vs}(t)$ is shown in the lower panel of Fig. 5. The exception for low alkali concentrations is a matter of phase behavior and will be discussed further below. For the range of favorable alkali concentrations (high recovery factor), the χ_{vs} indicates a strongly water-wet state.

It is noticeable that χ_{vs} show larger scatter for water flooding than for alkaline flooding. This is explained with the same argument we used to explain the scatter in the recovery data; if the system is dominated by large clusters with high volumes and many loops, then a single cluster, which may statistically not be represented in the observed domain, may dominate the recovery factor and the χ_{vs}. It appears to be even more sensitive to the REV than all the other quantities deduced in the frame of this work. This is the case after water flooding, but not after alkaline flooding, where we generally observe small clusters and a smooth dependency as a function of alkali concentration.

6 Lorenz analysis

The data presented so far, indicate a plateau of the recovery factor and the Euler characteristic as a function of the alkali concentration. The optimum can be found in a range between 1000 and 3000 ppm Na_2CO_3 with a mild decline to higher concentrations. Both quantities are

associated with uncertainties, which are a result of the investigated domain size versus the largest clusters, which are statistically not well represented in the domain.

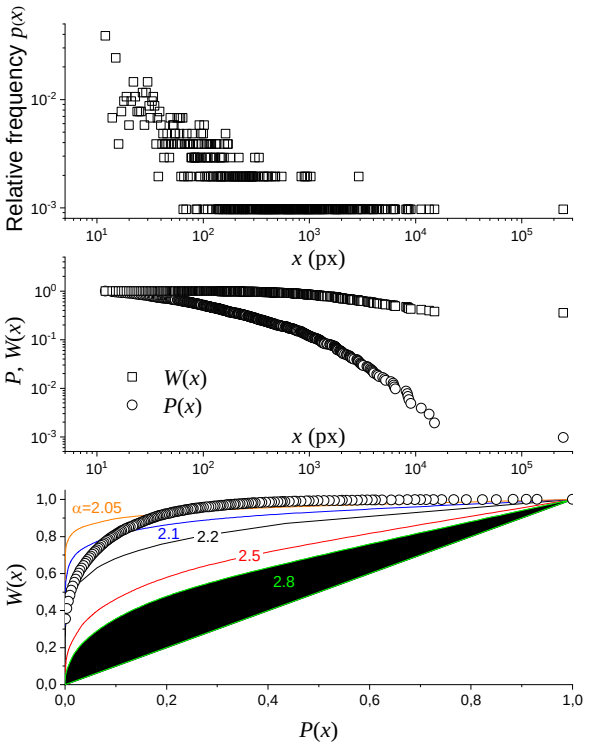

Fig. 8: Data taken from a water flood. Top: cluster volume distribution (CVD) ($\boldsymbol{p}$) (relative frequency as function of cluster size). Middle: cumulative CVD ($\boldsymbol{P}$) and volume weighted cumulative CVD ($\boldsymbol{W}$). Bottom: Lorenz plot $\boldsymbol{W(P)}$. For comparison, Lorenz plots for fractal distributions with different exponents $\boldsymbol{\alpha}$ are given in the same panel. The area under the curves, as indicated for $\boldsymbol{\alpha = 2.8}$, is a measure of "heterogeneity". In the present case, $\boldsymbol{P(x)}$ corresponds to the largest fraction of clusters, and $\boldsymbol{W(x)}$ to the total oil volume associated with this fraction of clusters. For fractal distributions: $\boldsymbol{W = P^{(\alpha-2)/(\alpha-1)}}$.

In contrast to the recovery factor and the Euler characteristic, the displacement characteristic may be more robustly reflected in the cluster size distribution, which is less sensitive to individual clusters at the tail end of the distribution. Fig. 8 illustrates various cluster-volume distribution plots as applied in the following to all data sets; the top row of Fig. 9 shows the cumulative cluster size distributions $P(x)$ at the end of the respective floods. The data were calculated from the cluster size distribution, $p(x)$, by integration [17, 18]:

$$P(x) = \int_x^\infty p(y)dy.$$

As a first observation, the results on water flooding (blue symbols) show a very consistent behavior despite the scatter in the recovery data and the Euler characteristic. Comparing the individual data sets to the subsequent alkaline floods, we find that $P(x)$ has a much narrower distribution to smaller clusters after alkaline flooding, consistent with the visual observations. Assuming for a moment a fractal distribution, $p(x) = cx^{-\alpha}$, an exponent α can be determined by a maximum likely hood approach [11, 17, 18]. In a double logarithmic plot, α appears as slope of a straight line fit, which is shown as lines in the upper row of Fig. 9; we find that α becomes generally larger after alkaline flooding, consistent with a narrower CVD, and deviates strongest in cases where we find high recovery and positive χ_{vs} and are rather similar for the cases we consider outside optimum. However, this signature is not very robust, because the range, over which the data show fractal behavior is about one order of magnitude and hence rather limited.

It is evident that the size of an individual cluster directly refers to (a) phase mobility (cluster length) and (b) to recovery (cluster volume). Therefore, an imbalance of the cluster size distribution to larger clusters may be beneficial for the mobilization of oil, i.e. there is a higher EOR potential. Such an imbalance may be described by Lorenz diagrams. This concept refers back to Max Otto Lorenz (1880–1962), who was a US Economist and described with his concept the distribution of wealth in society [19]; next to $P(x)$, we calculate the volume-weighted cluster size distribution by integration:

$$W(x) = \frac{\int_x^\infty yp(y)dy}{\int_{x_{min}}^\infty yp(y)dy},$$

with x_{min} being the lower bound of the distribution. Plotting $W\big(P(x)\big)$ results in the Lorenz plot. We translate the economic interpretation – P being the richest fraction of the population and W the associated fraction of the total wealth – to the problem of oil production – P being the largest fraction of clusters and W being the total volume of oil associated with this fraction of clusters. The closer the Lorenz curve tends to be a straight line (the diagonal), the more equal the oil is distributed over the different classes of clusters. The more the curve deviates from the diagonal to the upper left corner, the more the large clusters are dominating the oil volume – an imbalance of wealth.

We may associate larger clusters with higher EOR potential, since large clusters are easier to be mobilized, or, in the present case, may be subject to clusters breakup by viscous forces. The lower row of Fig. 9 compares the Lorenz plots after water flooding and alkaline flooding. We observe in all cases (but 200 ppm, where no change has been observed) a deviation of the Lorenz curve to a more uniform distribution due to alkaline flooding. Together with the decrease of absolute cluster sizes, this indicates a decrease in further EOR potential. The signature is most pronounced in the range where highest recovery and highest Euler characteristic is observed. The effect of alkaline flooding in the Lorenz plots appears to be a robust indication of a working EOR process, which can be quantified by the difference of the Lorenz factor of

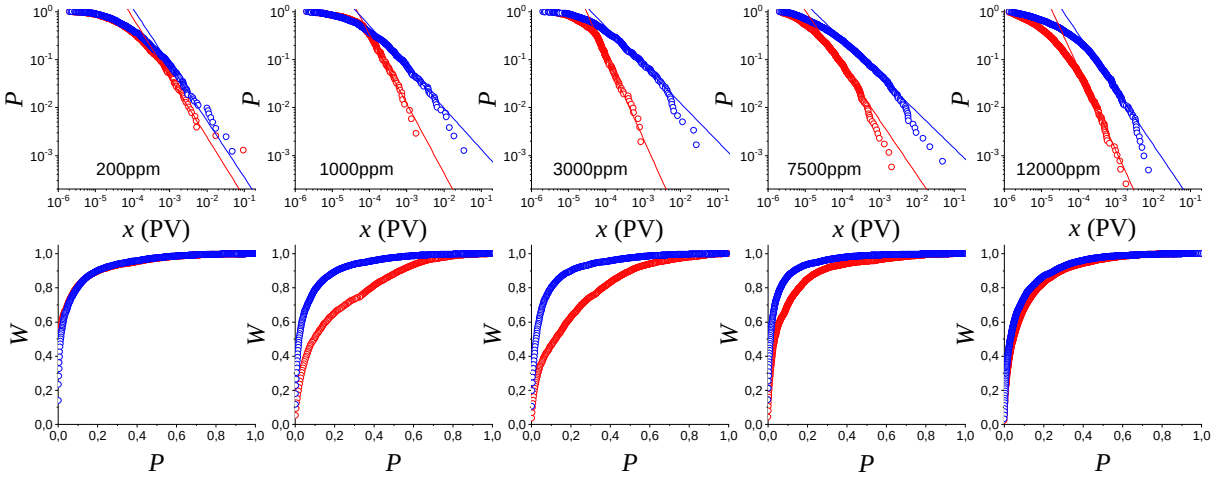

Fig. 9: Top row: cumulative cluster size distributions for three experimental sequences of water floods (blue) and alkaline floods (red) with 200, 1000, 3000, 7500 and 12000 ppm Na_2CO_3. The lines correspond to power law fits by a maximum likelihood approach. Bottom row: Lorenz plots for the same data sets.

water flooding and alkaline flooding ΔL, with $L = 2\left(\int_0^1 W dP - \frac{1}{2}\right)$, which varies in between $\Delta L = 0$ at 200ppm and $\Delta L = 0.12$ at optimum performance. Its dependency on the Na_2CO_3 concentration is compared to the recovery factor and the Euler characteristic in Fig. 6; it shows a stronger decline to higher concentrations than the other quantities and therefore defines the optimum better.

7 Texture of oleic and emulsion phases

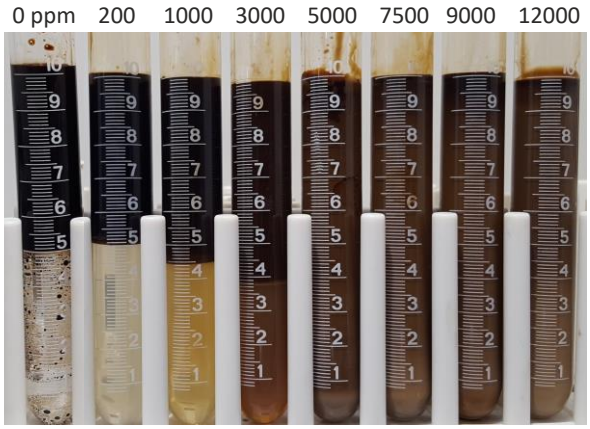

Fig. 10: Phase behavior after mixing crude 8 with water of different Na_2CO_3 concentrations in ppm as indicated in the picture.

Bringing the high-TAN oil (crude 8) in contact with an alkalic solution, the interfacial tension is lowered to a degree that emulsions are forming. This is shown in Fig. 10 for a series of experiments with different Na_2CO_3 concentrations in test tubes; the same volumes of crude oil and alkali solution were brought in contact to each other, the fluids were mixed by shaking the tubes and subsequently put for 48 h at rest. At rest and with time, the fluids separate by gravity to their equilibrium state and stable fluid phases may be observed. In the present case, oil-in-water and water-in-oil emulsions have been observed simultaneously as visible by a coloring of the aqueous phase and a decrease of the oil-water contact line, which indicates a swelling of the oil phase. No separate micro emulsion phases were observed in between the oleic and the aqueous phase as for optimized surfactant solutions, which may be a result of the variety of surfactants generated from the crude oil by saponification. The contrast between the oleic and the aqueous phase became gradually less with increasing alkali concentration; we may say, the degree of emulsification is monotonically increasing as function of C_{Na2CO3}.

In contrast, only water-in-oil emulsions were observed in the respective microfluidic experiments and this just to a limited extend. Examples of resulting textures are given in Fig. 11. Up to this point, emulsification has not been taken into account in the cluster analysis; the approach to identify the oil phase distribution, as discussed so far, is based on two-phase grey-scale image segmentation; we discriminated the light grey aqueous phase from a dark oil phase by essentially setting a threshold in between the respective grey values. With this approach, we ignore effects of emulsification. Different types of textures have been identified as a result of emulsification. We distinguish in the following between emulsions and conglomerates.

7.1 Effect of emulsification

In the presented series of experiments, emulsification was predominantly observed for rather low and high alkali concentrations and just to a minor extend in between. A possible explanation will be given below. Emulsion phases appear darker as the oil phase and become darker and expand in time. As can be seen in the lower left image of Fig. 11, the grey scale between emulsions and the oil phase changes gradually and a phase segmentation between them may not be useful. With the present segmentation approach, we partly ignore emulsion phases. This is because water participates in emulsions to a certain volume, which we account for as oleic phase – the oil phase is swelling. As a consequence, our material

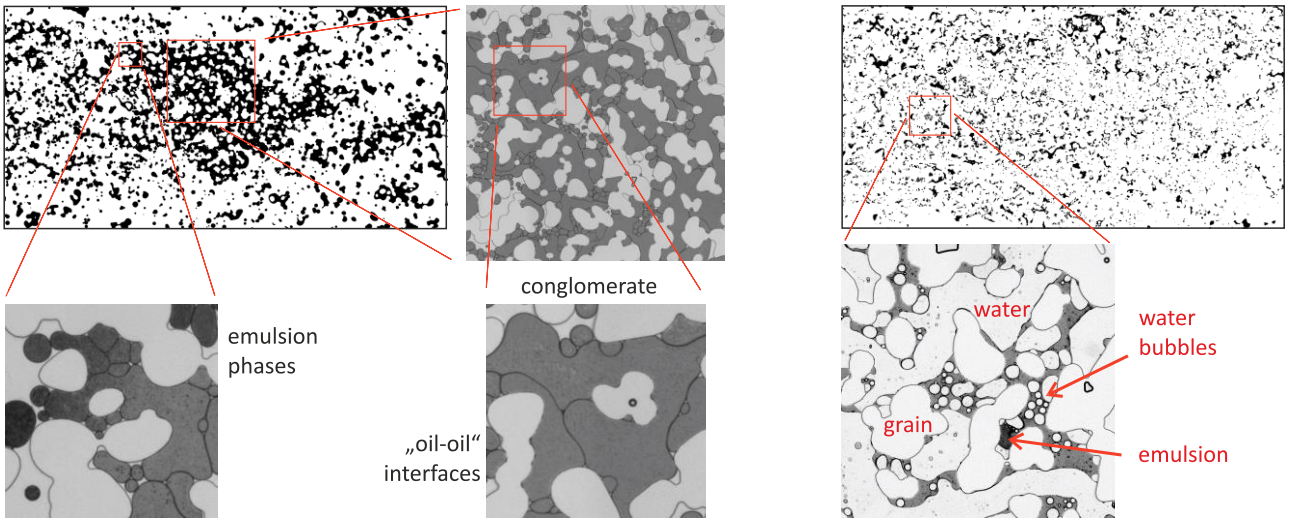

Fig. 11: Left side: segmented oil pattern after alkaline flooding with 200 ppm Na_2CO_3. The zoom in shows the formation of conglomerates and a detailed view on the observed "oil-oil" interfaces. The lower left image shows the boundary of the conglomerate with emulsion formation; darker grey values indicate water-in-oil emulsion phases. Right side: emulsion phases at 12000 ppm Na_2CO_3 concentration; the texture, respectively the various bubble sizes, makes it difficult to discriminate between emulsions and bubbles/clusters.

balance may not be perfect and the oil saturation may be slightly overestimated in the respective cases. We consider the associated error on the recovery curves as small. On the other hand, emulsions have been found to pin oil clusters, i.e., to demobilize the oleic phase; because emulsification influences cluster mobility, it is implicitly reflected (and accounted for) in the cluster topology and cluster statistics as given above.

7.2 Conglomerates

During displacements, mobile oil clusters may come into contact with each other. Depending on interfacial properties they may merge forming larger clusters. This has been observed in several pore scale displacement studies using model oils [4, 5, 20]. Such coalescence events have been observed for higher alkali concentrations (i.e. lower interfacial tension) in the current study. Sometimes, especially at low alkali concentrations, bubbles adhere together without merging. This is illustrated in Fig. 11; such conglomerates are stable configurations of oil droplets separated by dark appearing interfaces, which might be interpreted as emulsion. Even appearing to the eye as individual droplets, conglomerates may behave as large clusters with a highly negative χ_{vs}, even in cases that we would not call "oil wet". At that point it is too simple to talk about a single connected cluster or individual droplets. It also may be too simple to link the Euler characteristic to the wetting state, but still reflect phase connectivity. In Fig. 5, the Euler characteristic for two alternative interpretations of the 200-ppm experiment is given; (A) accounts for individual droplets, even if they form conglomerates, (B) treats conglomerates as objects. Conglomerates may be exceptional and leaving room for interpretation with respect to cluster size distribution and χ_{vs}, depending on whether they are accounted for as individual small clusters, or rather as super cluster (as we do).

7.3 Emulsification at low and high ppm – a hypothesis

It is quite remarkable that emulsification was observed for high and low alkali concentration, but not for concentrations in between that we consider as optimum condition – emulsification and the recovery factor behave non-monotonic. This in contradiction to the phase behavior experiments shown in Fig. 10 in which the degree of emulsification is monotonically increasing as function of C_{Na2CO3}. Emulsion phases are known to influence displacements due to various aspects; Emulsions may facilitate ultra-low interfacial tension between oil and brine, improving the displacement efficiency. On the other hand, emulsions have typically a substantially higher viscosity than their constituents, which may oppose displacement.

A first attempt to understand the degree of emulsification in the present case requires to consider not only the bulk phase behavior, but also the flow regimes: At *low alkali concentrations*, the displacement efficiency is not much improved compared to the preceding water flood and just a minor fraction of the remaining oil is mobilized; most of the oil clusters are stagnant. These clusters are contacted by multiple PVs of alkali solution and over time, emulsions are forming, pinning the clusters even more due to the increasing viscosity of the oleic phase by emulsification. At very *high alkali concentrations*, emulsification is fast – faster than the mobilization of the clusters. Emulsions are forming nearly instantaneously, pinning the oil phase by the low mobility of the emulsion phase at the boundaries of the oil clusters. At a certain degree of emulsification, the oleic phase becomes stagnant (trapped). For concentrations in between – *at optimum conditions* – the alkali concentration is high enough to mobilize the oil, but not too high to lead to fast emulsion formation. Once mobilized, oil droplets move with the injection water and the droplet does no come in

contact with multiple PVs as in case of a stagnant oil phase – the relative velocity between the mobile oil clusters and the injection water may be close to zero.

8 Summary and conclusions

In the present study, we use microfluidics as a screening tool to optimize the composition of injection water for alkaline flooding. We use the high spatial and temporal resolution to study the respective displacement processes and changes in the displacement efficiency on the pore scale. Due to the limited size of the flooding domain, the recovery factor alone is not a sufficient criterion for evaluating displacements. This is especially true for the results of water flooding, where the remaining oil phase consists of relatively large-volume clusters that dominate the system. To make robust predictions, we analyze the remaining oil phase based on its steady-state cluster size distribution and Euler characteristic at the end of each flood.

What are the signatures of an ideal alkaline flood or – more general – an ideal EOR displacement? By changing the capillary number, larger clusters break up into smaller clusters. It has been observed that these smaller clusters are non-wetting and mobile. On this basis, we define the EOR potential: (1) the initial cluster size distribution (volume distribution) shows a strong imbalance toward large clusters. As a measure of this imbalance we use Lorenz diagrams and for quantification the Lorenz factor, and (2) in the present case, the large clusters are predominantly pinned to the solid phase, i.e. being in a wetting state. To analyse the wetting state, we introduced a volume weighted Euler characteristic. These statistical and topological phase properties may change from water flooding to the subsequent alkaline flooding; on this basis we optimize the injection water composition. We find the following criteria: The system lowers its EOR potential, which is reflected in the following factors:

- a high tertiary recovery factor is reached on a short time scale,
- the tendency for a positive volume-scaled Euler characteristic that reflects water-wet condition,
- the tendency to smaller clusters, which are reflected in a narrower cumulative cluster-volume distribution, and
- a more even distribution of oil cluster volumes, which tends to reflect a lower Lorenz factor.

Using these criteria and for the present case, a plateau with optimum alkali concentration around 3000 ppm Na_2CO_3 has been identified. Interestingly, no significant emulsification was observed in this range, which stays in contrast to the classical phase-behavior experiments performed with the same fluid pairs. Outside this optimal EOR range, emulsification was observed, interestingly for higher *and* lower alkali concentrations. A first attempt of explanation was made on the basis of the alkali concentration and the contact time based on droplet/cluster mobility.

The authors acknowledge the OMV AG, Vienna, Austria for funding this project. Furthermore, we would like to thank Ryan Armstrong for insightful discussions on fluid topology and Hassan Mahani, Steffen Berg and Hendrik Rohler for reviewing and commenting the manuscript.

References

1. L. W. Lake, *Enhanced oil recovery*. Prentice Hall, 1989.
2. G. Hirasaki, C. A. Miller, and M. Puerto, "Recent Advances in Surfactant EOR", *SPE Journal*, vol. 16, no. 04, pp. 889-907, 2011.
3. A. A. Olajire, "Review of ASP EOR (alkaline surfactant polymer enhanced oil recovery) technology in the petroleum industry: Prospects and challenges", *Energy*, vol. 77, pp. 963-982, 2014.
4. S. Berg *et al.*, "Onset of Oil Mobilization and Nonwetting-Phase Cluster-Size Distribution", *Petrophysics*, vol. 56, no. 01, pp. 15-22, 2015.
5. M. Rücker *et al.*, "From connected pathway flow to ganglion dynamics", *Geophysical Research Letters,* vol. 42, no. 10, pp. 3888-3894, 2015.
6. V. A. Lifton, "Microfluidics: an enabling screening technology for enhanced oil recovery (EOR)", *Lab on a Chip,* vol. 16, no. 10, pp. 1777-1796, 2016.
7. E. Unsal, M. Broens, and R. T. Armstrong, "Pore Scale Dynamics of Microemulsion Formation", *Langmuir,* vol. 32, no. 28, pp. 7096-7108, 2016.
8. W.-B. Bartels, H. Mahani, S. Berg, R. Menezes, J. A. van der Hoeven, and A. Fadili, "Oil Configuration Under High-Salinity and Low-Salinity Conditions at Pore Scale: A Parametric Investigation by Use of a Single-Channel Micromodel", *SPE Journal*, vol. 22, no. 05, pp. 1362-1373, 2017.
9. M. Broens and E. Unsal, "Emulsification kinetics during quasi-miscible flow in dead-end pores", *Advances in Water Resources*, vol. 113, pp. 13-22, 2018.
10. S. Iglauer, S. Favretto, G. Spinelli, G. Schena, and M. J. Blunt, "X-ray tomography measurements of power-law cluster size distributions for the nonwetting phase in sandstones", *Physical Review E,* vol. 82, no. 5, p. 056315, 2010.
11. A. Georgiadis, S. Berg, A. Makurat, G. Maitland, and H. Ott, "Pore-scale micro-computed-tomography imaging: Nonwetting-phase cluster-size distribution during drainage and imbibition", *Physical Review E,* vol. 88, no. 3, p. 033002, 2013.
12. R. T. Armstrong, A. Georgiadis, H. Ott, D. Klemin, and S. Berg, "Critical capillary number: Desaturation studied with fast X-ray computed microtomography", *Geophysical Research Letters,* vol. 41, no. 1, pp. 55-60, 2014.
13. R. T. Armstrong, J. E. McClure, M. A. Berrill, M. Rücker, S. Schlüter, and S. Berg, "Beyond Darcy's law: The role of phase topology and ganglion dynamics for two-fluid flow", *Physical Review E,* vol. 94, no. 4, p. 043113, 2016.

14. R. T. Armstrong *et al.*, "Porous Media Characterization Using Minkowski Functionals: Theories, Applications and Future Directions", *Transport in Porous Media*, 2018.
15. J. E. McClure *et al.*, "Geometric state function for two-fluid flow in porous media", *Physical Review Fluids,* vol. 3, no. 8, p. 084306, 2018.
16. M. Borji and H. Ott, "suppl. material", 2019.
17. A. Clauset, C. R. Shalizi, and M. E. J. Newman, "Power-Law Distributions in Empirical Data", *SIAM REVIEW,* vol. 51, no. 4, pp. 661-703, 2009.
18. Y. Virkar and A. Clauset, "Power-law distributions in binned empirical data", *The Annals of Applied Statistics*, vol. 8, no. 1, pp. 89-119, 2014.
19. M. O. Lorenz, "Methods of Measuring the Concentration of Wealth", *Publications of the American Statistical Association,* vol. 9, no. 70, pp. 209-219, 1905.
20. S. Youssef *et al.*, "Oil ganglia dynamics in natural porous media during surfactant flooding captured by ultra-fast X-ray microtomography", International Symposium of the Society of Core Analysts, SCA2014-023, 2014.